Spatiotemporal Mapping of a Photocurrent Vortex in Monolayer MoS_2 Using Diamond Quantum Sensors

Brian B. Zhou[1,2,*,†], Paul C. Jerger[1,*], Kan-Heng Lee[1,3], Masaya Fukami[1], Fauzia Mujid[4], Jiwoong Park[1,4], David D. Awschalom[1,5,†]

[1] *Pritzker School of Molecular Engineering, University of Chicago, Chicago, Illinois 60637, USA*

[2] *Department of Physics, Boston College, Chestnut Hill, Massachusetts 02467, USA*

[3] *School of Applied and Engineering Physics, Cornell University, Ithaca, NY 14853, USA*

[4] *Department of Chemistry and James Franck Institute, University of Chicago, Chicago, Illinois 60637, USA*

[5] *Center for Molecular Engineering and Materials Science Division, Argonne National Laboratory, Lemont, Illinois 60439, USA*

[*] *These authors contributed equally to this work.*

[†] email: *brian.zhou@bc.edu, awsch@uchicago.edu*

Supplementary Information Contents

Section 1: Experimental Setup

The substrates used in this experiment are [001]-oriented electronic-grade type IIa diamond (Element Six), and are 2x2x0.5 mm in size. The diamond and MoS_2 samples were cooled in a closed-cycle helium cryostat (Montana Instruments) with a base temperature of T_D = 6 K, and imaged in a purpose-built confocal microscopy setup containing an in-cryo objective with NA = 0.9 and 100X magnification (Olympus MPLFLN100x). A permanent magnet mounted on a translation stage provided magnetic fields between 100 and 500 G, with misalignment to the selected NV axis of 1-4° depending on field (2° typical). Initialization and readout was performed with a 532-nm solid state laser (Elforlight), while microwave pulses were delivered by a wire coil suspended above the sample surface.

The MoS_2 was optically excited using a 661.5 nm laser diode (Thorlabs LP660-SF20), initially gated by an acousto-optic modulator (Gooch & Housego). It was then pulsed using a combination of free-space electro-optic modulator (ConOptics 350-160, rise time ~8 ns) and Glan-Thompson polarizer, and its polarization was set with a Soleil-Babinet compensator (Thorlabs). However, the effects described in the paper showed no dependence on the excitation polarization. This excitation was coupled into the main optical path using a dichroic with a 685 nm cutoff (Semrock Di03-R685).

For most of the data presented in the main text, the red laser was purposely misaligned from the green laser; by impinging on the back aperture of the microscope objective from a slightly different angle, the red could be targeted to a different area of the sample than the green excitation. To determine the spatial separation of the red and green spots, the reflections off the sample surface were imaged using a pellicle beamsplitter and an Edmund Optics camera (UI-154xSE-C). The laser spots at low power were fit to Gaussian distributions to determine center locations, and relative distances were calibrated by imaging a 1951 USAF Resolution Test Target (Thorlabs). We found an image pixel size of 95 nm, and a center measurement repeatability of ±50 nm.

The microwave signal generator, optical modulators, and single-photon counting hardware were controlled and coordinated by an arbitrary waveform generator (AWG; Tektronix 5014C, 1 GSample/s). For the data in Fig. 6 of the main text, where the optical excitation was desynchronized from the sensing sequence, the optical modulation was controlled by a function generator (Agilent 33220A) instead of the AWG. NV center emission was collected between 690 and 830 nm with additional filters, and measured by an avalanche photodiode (PerkinElmer SPCM-AQR-16-FC). For the XY8 sequences, the 532 nm readout and initialization laser was turned on for 4 μs during each measurement cycle, with readout counts collected during the first 1 μs. The 532 nm optical power was 100 μW.

The spectrum shown in Fig. 1f of the main text was taken on two samples mounted side-by-side on a single sample holder: 1) a third diamond sample with identical implantation conditions as the primary sample used in our photocurrent measurements, but with no MoS_2 coverage, and 2) a monolayer sample of MoS_2 on a silicon substrate. The monochrometer used was a Princeton Instruments Acton SP-2750 with an Andor iStar 334T ICCD camera. Resolution was set to 1 nm. The diffraction grating had 300 gr/mm and a blaze wavelength of 750 nm. On both scans, the sample was excited with 532 nm light, the signal was filtered below 605 nm (Semrock Di02-R594-25x36), and a successive background scan was then subtracted.

Section 2: 1L-MoS_2 Sample Synthesis and Vacuum Transfer

Growth of monolayer (ML) transition metal dichalcogenide (TMD) films. Wafer scale monolayer (ML) films of MoS_2 were grown by metal organic chemical vapor deposition (MOCVD) [1]. Molybdenum hexacarbonyl (MHC) and diethyl sulfide (DES) were selected as chemical precursors for Mo and S, and introduced into a tube furnace in gas phase. H_2 and N_2 were injected to the growth chamber using separate lines. The optimum growth parameters for ML TMD films are as follows. We used a total pressure of ~ 10 Torr, growth temperature of 550 ^oC and growth time of 26 hrs. The flow rates of precursors are 0.01 sccm for MHC, 0.4 sccm for DES, 5 sccm for H_2, and 150 sccm for N_2, which were regulated by individual mass flow controllers (MFCs). NaCl is loaded in the upstream region of the furnace, which increases the grain size and monolayer yield. The physical, optical and electrical properties of the films used in the current NV center experiments are similar to that reported in our prior work [1].

Vacuum transfer of MoS_2 monolayer onto diamond substrate. Here we used our previously devised vacuum transfer method [2] that minimizes contamination from air or any wet solution at the interface between the MoS_2 monolayer and diamond substrate. We first spin-coated the supporting polymer layer poly-methyl methacrylate (PMMA, 495k, 8% in anisole) onto the as-grown MoS_2 monolayer sitting on its growth substrate SiO_2/Si. The spin-coat parameter was 60 seconds at 3000 rpm and the PMMA was then baked at 180 ^oC for 10 minutes. Afterwards, we attached a thermal release tape (TRT, manufactured by Nitto-Denko) with a hole cut out at the center. The TRT served as the removable handling frame for the rest of the process. We then mechanically peeled the PMMA/MoS_2 off the SiO_2/Si without the use of any chemicals or etchants, which kept the bottom surface of the MoS_2 clean.

Next, the diamond substrate and the suspended PMMA/MoS_2 on TRT were mounted into a vacuum chamber [2]. The chamber was pumped down to below 70 mTorr and the diamond substrate was heated to 100 ^oC, before which the PMMA/MoS_2 was pressed onto the diamond substrate using a vacuum feedthrough manipulator. Here, our diamond substrate size was smaller than the size of the hole in the TRT, and therefore, only the PMMA/MoS_2 was stuck onto the diamond. The pressing continued for five minutes to allow enough time for the MoS_2 to stick to the diamond. After that, the TRT handling layer was removed from the PMMA/MoS_2/diamond sample in ambient conditions. The PMMA was finally removed by immersing the sample in hot acetone for one hour.

For the sample shown in Fig. 1d of the main text, we additionally attached another TRT on half of the sample area after the vacuum transfer but before removing PMMA, and then again mechanically peeled the TRT off the substrate to remove the PMMA/MoS_2 from the substrate. The PMMA/MoS_2 not covered by TRT remained strongly stuck on the diamond, generating both MoS_2 on diamond and bare diamond area on a single chip for control measurements. A total of 3 ML samples were transferred and measured for this paper using two diamond substrates of different NV implantation depths. All three samples demonstrated the photocurrent effect.

MoS_2-diamond interface. Atomic force microscopy (AFM) was used to characterize the flatness of MoS_2 on diamond substrates. The bare diamond substrates have a surface roughness (rms) of approximately 0.3 nm. With MoS_2 transferred, the roughness increases only slightly, with values between 0.6-1.2 nm depending on sample age, and no bubble-like features are observed over extended areas. Older samples show increased roughness due to uneven oxidation of the MoS_2

layer. An AFM scan of an older sample is shown in Fig. S1a, indicating a smooth transfer. However, for samples which have been cooled down to 6 K, nanometer-scale wrinkles appear in successive, room-temperature AFM scans (Fig. S1b). These wrinkles pervade the layer, and have previously been observed to appear when a 2D material with a different thermal expansion coefficient (TEC) than its substrate is cooled or heated [3]. In this case, the diamond substrate [4] has a smaller TEC than the MoS_2 [5], causing the MoS_2 layer to relatively shrink during cooldown. The wrinkles observed in Fig. S1b are then expected to appear as the sample warms to room temperature, and thus they may not be present during low-temperature measurements for the initial cooldown.

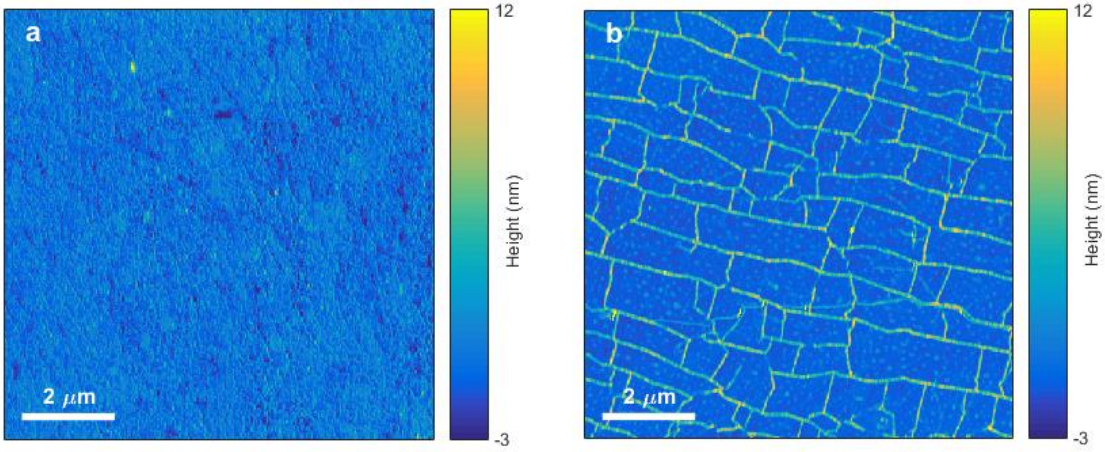

Fig. S1. a-b) AFM scans of monolayer MoS_2 after transfer to two different diamond substrates, plotted on the same scale. a) Scan of a sample prior to any cooling below room temperature. Surface roughness of the area is 1.2 nm, increased by oxidation of the MoS_2 over time. b) Scan of a sample after two cycles of cooling to 6 K and warming to room temperature. 5-10 nm wrinkles appear due to differential thermal expansion between diamond and MoS_2. Surface roughness of the area is 2.2 nm, or 0.6 nm excluding the wrinkles.

Section 3: NV Ensemble Sample Preparation and Characterization

To create near-surface NV center ensembles in the diamond samples, ^{15}N ions were implanted (CuttingEdge Ions, LLC) with an area dose of $10^{12}/cm^2$. This yielded ~85 NV centers per optical spot size, as determined through comparison to the fluorescence from a single NV center at the same optical power. The primary results reported were from a sample implanted at an energy of 30 keV (approximately 40 nm deep, via SRIM). Monolayer MoS_2 was transferred twice to this sample, and data presented in main text correspond to the first transfer (Device A), while some data from the second transfer is shown in the SI (Device B). Additionally, photocurrent detection was confirmed on a third device (Device C) using a diamond sample implanted at 15 keV (~20 nm). Implantation was performed at 7° from surface normal to avoid channeling effects.

After implantation, the samples were initially annealed at 850 °C for 4 hrs in argon forming gas to mobilize vacancies and create NV centers. A second annealing treatment was performed to annihilate excess vacancy complexes, consisting of 800 °C for 6 hrs followed by 1100 °C for 2 hrs, all in argon forming gas [6]. The measured ensemble Hahn-echo T_2 time at room temperature increased by roughly a factor of 4 as a result of the high-temperature anneal, from ~8 μs to ~34 μs, varying between samples and locations. To oxygen-terminate the diamond surface, the samples were then placed in a 1:1 mixture of concentrated sulfuric and nitric acids, heated to 225 °C, for 2 hrs.

At cold temperatures, on a region covered by MoS_2, the dephasing time T_2^* of the deeper ensemble (~40 nm) was 0.51 ± 0.08 μs (Fig. S2a-b). $T_{2,\,Hahn}$ increased to 118 ± 8 μs (Fig. S2c). For the shallower ensemble, $T_{2,\,Hahn}$ was measured to be only 27.4 ± 1.2 μs, indicating that this sample may still be limited by surface proximity. No difference in $T_{2,\,Hahn}$ was measured between regions of bare diamond and those covered by MoS_2. We performed a coherence measurement for the XY8-2 sequence (16 rephasing pulses) on the deeper sample, and by fitting a stretched exponential, ^{13}C revivals, and a slow modulation due to field misalignment, determined the coherence time was extended to 235 ± 12 μs (Fig. S2d). Higher-order XY8 sequences would

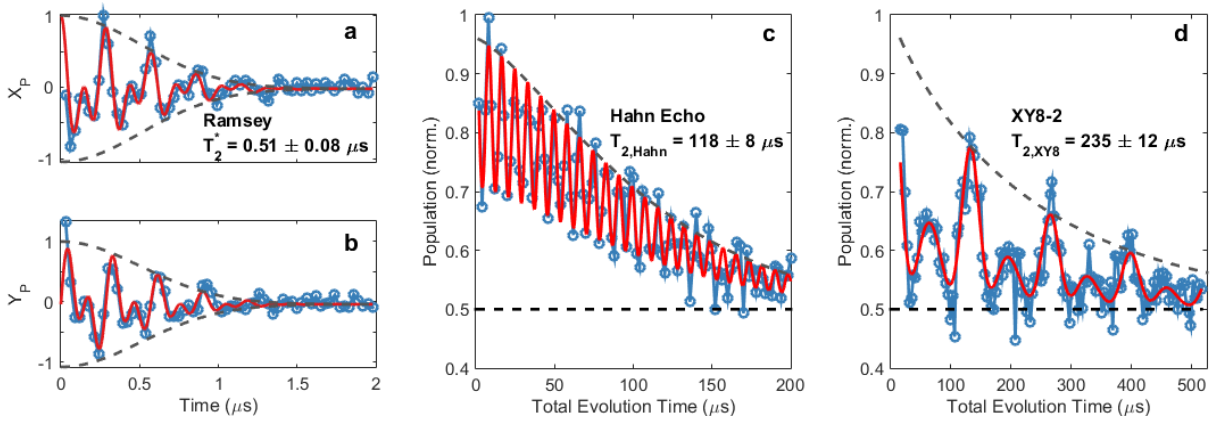

Fig. S2. Coherence properties of NV ensemble sample (30 keV implantation energy) used in photocurrent measurements (T_D = 6 K). a-b) Ramsey measurement with 5 MHz detuning. Two modulation frequencies appear due to the spin-1/2 ^{15}N. Decay envelope is T_2^* = 0.51 ± 0.08 μs. c) Hahn echo measurement at 226 G. Fit includes ^{13}C revivals and envelope fits $T_{2,\,Hahn}$ = 118 ± 8 μs. d) Coherence decay for XY8-2 sequence. Fit function is a stretched exponential that is modulated by ^{13}C revivals and field misalignment. $T_{2,\,XY8}$ = 235 ± 12 μs.

show even longer coherence times, though our total sensing sequence time was typically no longer than 150 μs.

When at room temperature but under vacuum, the regions of our NV ensemble sample covered by MoS_2 showed comparable fluorescence to bare diamond regions (after filtering out the MoS_2 A-exciton peak). However, at cryogenic temperatures, the MoS_2 regions showed significantly higher fluorescence (Fig. S3a) as well as bleaching (Fig. S3b-c). The bleaching occurred rapidly during 532-nm excitation, yet slowly or not at all under 662-nm excitation at comparable optical powers. Fluorescence bleaching recovered very little or not at all in the dark, over the course of hours to days. We attribute these effects to fluorescence from gases adsorbed during or after the cooldown process (despite vacuum pressures below $1*10^{-5}$ Torr at the start of cooldown). Laser excitation then either partially desorbs these gases or quenches their fluorescence. Thus, even after bleaching, we cannot rule out that residual absorbed gases remain attached to surface of monolayer MoS_2. Bleaching over areas of diamond not covered by MoS_2 was not significant.

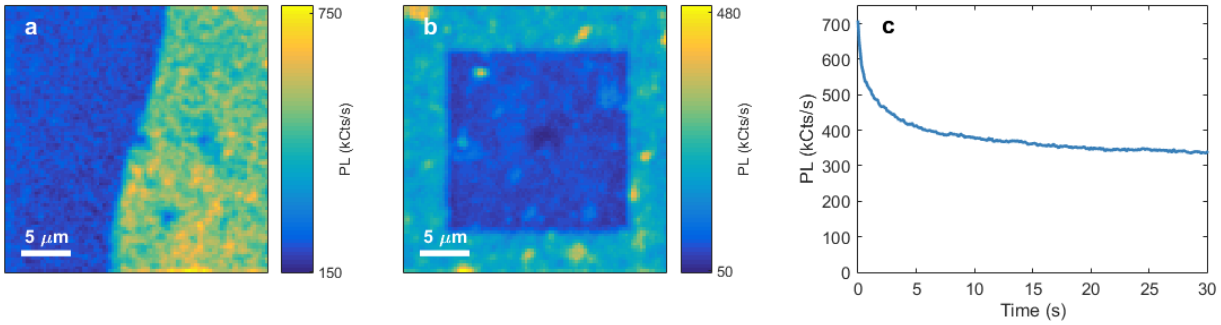

Fig. S3. a-b) Confocal scans of NV ensemble sample covered by monolayer MoS_2. Photoluminescence, PL. a) Boundary between bare diamond and MoS_2-covered sample at 6 K. MoS_2 is on the right half. b) Observation of photobleaching at 6 K. The central 20x20 μm area was scanned with 532 nm illumination for several minutes. Bright spots are contamination on the surface. Lower optical power was used here relative to (a), resulting in lower PL. c) Time dependence of photobleaching at a single location. Optical power ~25 μW.

Section 4: Data Analysis

As shown in Fig. 2a of the main text, the XY8-*N* sensing sequence consists of 8N+2 pulses: $\left(\frac{\pi}{2}\right)_y - \left[\pi_y - \pi_x - \pi_y - \pi_x - \pi_x - \pi_y - \pi_x - \pi_y\right]^N - \left(\frac{\pi}{2}\right)_{proj}$, where *x* and *y* indicate the axis on the Bloch sphere to rotate around. The π pulses are uniformly spaced by the interval τ, whereas the $\pi/2$ pulses are spaced by $\tau/2$. The rotation axis of the final $\pi/2$ pulse determines which projection of the spin $\{\pm X, \pm Y\}$ is measured by optical readout. Rotating around both *x* and *y* decouples the superposition from noise around both axes, and the pattern of interleaved *x* and *y* pulses is robust against pulse errors.

4.1 Pulse shape model

The XY8-N sequence is a multi-pulse extension of the simple Hahn echo sequence. Each π-pulse inverts (flips the sign of) the phase of the superposition state up to that point. For the single pulse Hahn echo, the phase acquired before the π-pulse will cancel the phase after the π-pulse for a dc field: i.e., the field is effectively multiplied by a Heaviside function that switches from -1 to 1 and is then integrated. For the XY8 sequence, there are simply more periods for this modulation function, switching sign each time a π-pulse is applied (Fig. 2b of the main text). Changing the rotation axis of the π-pulse between the *X* and *Y* axes makes the sequence robust to pulse errors. Making the sequence longer by repeating *N* times scales the acquired phase linearly (Fig. 3c, inset), as well as enables more stringent cancellation of fields with frequencies not commensurate with the modulation function (i.e., the frequency selectivity of the sequence becomes sharper). This reduces the bandwidth of noise that affects the NV center, extending its coherence time.

Due to the π-pulses applied to the NV center spin, total phase acquired for the XY8 sequence will be the time integral of the magnetic field $B_{\parallel}(t)$ along the NV axis multiplied by a modulation function $M(t)$:

$$\phi = \int_{t_0}^{t_0+8\,N\,\tau} 2\pi\gamma\, B_{\parallel}(t)\, M(t - t_0)dt,$$

where γ is the gyromagnetic ratio (2.8 MHz/G), $t_0 = \tau\,(\theta/180°)$, and $M(t)$ is:

$$M(t/\tau) = \begin{cases} -1 & for\ 0 \le\ mod(t/\tau - 0.5\,, 2) < 1 \\ +1 & for\ 1 \le mod(t/\tau - 0.5\,, 2) < 2 \end{cases}$$

The above parametrization is such that for $\theta = 0$, the π-pulses occur at half-integer values of τ. A schematic of the modulation function is shown in Fig. 2b of the main text.

We now consider a simple model of the XY8 response using pulse shapes with exponential rising and falling edges, motivated by common thermal dynamics and confirmed in simulation (Appendix D). We consider $B_{\parallel}(t)$ with equal rise and fall times τ_{rise}:

$$B_{\parallel}(t) = \begin{cases} \left(1 - e^{-\frac{t}{\tau_{rise}}}\right)(1 - C_0)^{-1} & 0 \le mod(t, 2\tau) \le \tau \\ \left(e^{-\frac{(t-\tau)}{\tau_{rise}}} - C_0\right)(1 - C_0)^{-1} & \tau \le mod(t, 2\tau) \le 2\tau \end{cases}$$

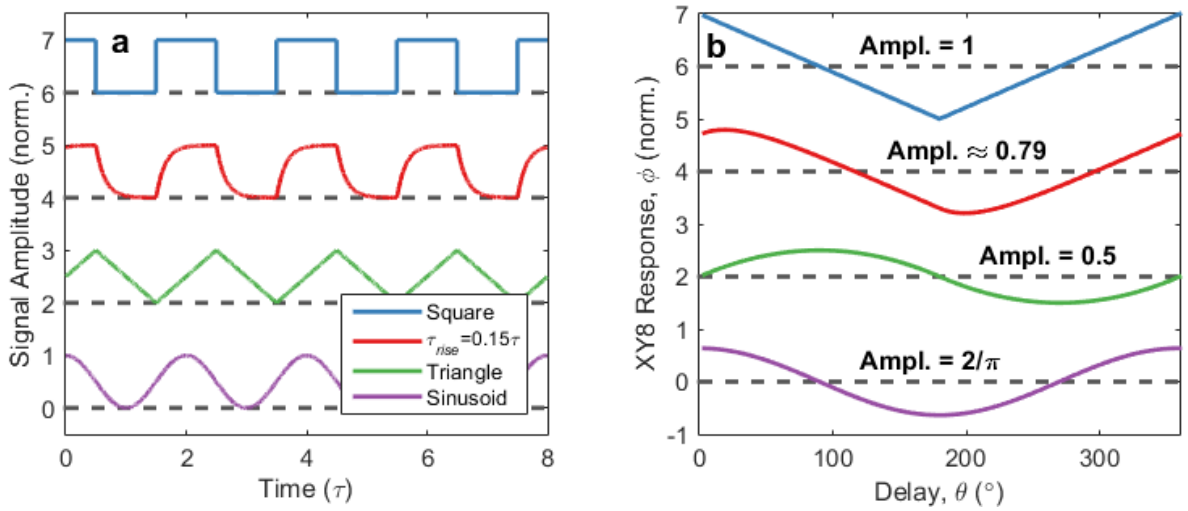

Fig. S4. a) Traces of sample signals synchronized to an XY8-1 sensing sequence. For $\theta = 0$, NV π-pulses are applied at half-integer values of τ, concurrent with the square signal jumps. The second trace has an exponential rise and fall behavior with equal time constant τ_{rise}. All traces are normalized (i.e., $B_{max} = 1$). b) The phase acquired by the XY8 sequence, ϕ, for the sample signals in a). The sinusoid response is exactly sinusoidal. The exponential and triangle responses can be approximated with sinusoids, and exhibit a smaller maximum ϕ and a phase offset (θ_{opt}) relative to the ideal square pulses. The triangle wave signal achieves the maximum θ_{opt} of 90°. The maximum value of the acquired phase, $\phi(\theta_{opt})$, is denoted as "Ampl."

Here, $C_0 \equiv e^{-\tau/\tau_{rise}}$ is a constant introduced to normalize the pulse maximum. This isolates the effect of the pulse shape from the amplitude. Several representative traces are shown in Fig. S4a. If $\tau_{rise} = 0$, the pulse shape is a square wave; if $\tau_{rise} \rightarrow \infty$, the pulse shape approaches a triangle wave.

The phase acquired by the NV center can be computed by a piecewise time-integral for ϕ, as a function of relative timing θ between the modulation function $M(t, \theta)$ and signal field $B_{\parallel}(t)$. For square signal pulses synchronized to the frequency of the XY8 π-pulses (Fig. S4a, top trace), the sensor will accumulate maximum phase when the π-pulses occur exactly when the square wave turns on or off ($\theta = 0$). In this case, the Heaviside-like modulation function $M(t)$ exactly coincides with the square pulses, and all *B*-field pulses are constructively integrated. For $\theta = \pi/2$, the sensor accumulates no phase even for large signal amplitudes, since the $M(t)$ changes sign exactly halfway through each *B*-field pulse, resulting in cancellation in the integral. For intermediate and long rise times, we can derive the response of the acquired phase ϕ versus the delay θ and plot the results in Fig. S4b. Two aspects are apparent:

1. The absolute value of the maximal accumulated phase Φ diminishes as the rise time τ_{rise} increases. This occurs because the rise time spreads out the pulse area across the modulation function, resulting in partial signal cancellation even at the optimal delay θ_{opt}. We define the time averaged value of the magnetic field sensed by the NV center (normalized by the duty cycle of the excitation pulses) by $B_{avg}(\theta) = \frac{\phi(\theta)}{\gamma 4N\tau}$. Alternatively, the maximum value of the magnetic field at the end of the excitation pulse is denoted as B_{max}, which in this simulation is equal to 1 for all pulse shapes by construction.

For the square wave, it is clear that the maximal field B_{max} is equal to the time-averaged *B*-field at the optimal delay: $B_{max} = B_{avg}(\theta_{opt}) = \frac{\Phi}{\gamma 4N\tau}$. For other pulse shapes, we define the proportionality factor $\beta = B_{max}/B_{avg}(\theta_{opt})$. The ratio of B_{max} to $B_{avg}(\theta_{opt})$ is $\beta = \frac{1}{0.79} \approx 1.25$ for $\tau_{rise} = 0.15\tau$ and $\beta = \frac{1}{0.5} = 2$ for $\tau_{rise} \to \infty$.

2. The delay θ_{opt} for which the maximal accumulated phase Φ occurs increases as the rise time increases. This produces the maximum temporal overlap of the modulation function with the photocurrents, which effectively lag behind the excitation pulses. The triangle signal makes this disparity most evident, and also achieves the maximum delay in this model of 90°.

The behaviors of β and θ_{opt} are shown in Fig. 7 of Appendix C.

4.2 Phase accumulation fitting functions

The color of the RF pulse in Fig. 2a denotes the axis on the Bloch sphere for the spin rotation (blue: +*Y* axis, yellow: +*X* axis). The last $\pi/2$ rotation (gray) can be around either the $\pm X$ or $\pm Y$ axes to allow us to measure the X_P and Y_P projections of the final state in differential mode. For example, X_P is measured by subtracting the count-rate of the NV center after a final $\left(\frac{\pi}{2}\right)_{-Y}$ projection pulse from that for the $\left(\frac{\pi}{2}\right)_{+Y}$ pulse:

$$R_{-Y}(\pi/2)\begin{bmatrix}x\\y\\z\end{bmatrix} = \begin{bmatrix}0 & 0 & -1\\0 & 1 & 0\\1 & 0 & 0\end{bmatrix}\begin{bmatrix}x\\y\\z\end{bmatrix} = \begin{bmatrix}-z\\y\\x\end{bmatrix}$$

$$R_{Y}(\pi/2)\begin{bmatrix}x\\y\\z\end{bmatrix} = \begin{bmatrix}0 & 0 & 1\\0 & 1 & 0\\-1 & 0 & 0\end{bmatrix}\begin{bmatrix}x\\y\\z\end{bmatrix} = \begin{bmatrix}z\\y\\-x\end{bmatrix}$$

Our PL intensity then measures the Z_P projection of the qubit, which physically represents the population difference between the two basis states $|0\rangle$ and $|-1\rangle$. The count differences between the differential projection pulses ($\pm X$ or $\pm Y$) are then normalized by the same measurement for the identical XY8-*N* sequence, but with the red excitation laser completely off (no photocurrents). This accounts for background changes in coherence due to T_2 or precession of the ^{13}C bath when the total duration of the sensing sequence is changed. We avoid pulse spacings τ corresponding to minima in the NV center coherence caused by the ^{13}C bath (Fig. S2d).

We use the measurements of X_P and Y_P to determine the phase accumulated, since these projections of the final quantum state are given by $X_P = \cos\phi$ and $Y_P = \sin\phi$. For the sinusoidal signal,

$$\phi(\Phi, \theta) = \Phi\cos\theta,$$

where $\theta = 0$ is defined to be where the sensing sequence and signal are in phase. As described in Section 4.1, to apply this model to square excitation pulses with exponential rise and fall, two additional parameters (β and θ_{opt}) are introduced into the fit. Without prior knowledge of the rise time, we sweep θ to fit Φ and θ_{opt}. We simultaneously fit two data sets:

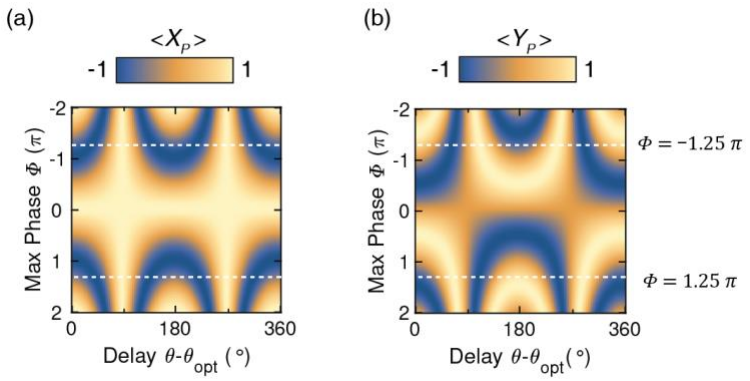

***Fig. S5*.** Expected dependence of the final NV spin projections X_P (a) and Y_P (b) on the delay θ (horizontal axis) and the maximum phase Φ acquired at the optimal delay θ_{opt} (vertical axis). The sign and magnitude of Φ are determined by the direction and magnitude of the local photocurrents. The dashed lines indicated the behavior for $\Phi = \pm 1.25\,\pi$, close to the data presented in Fig. 3a,b of the main text for an optical power of 25 μW. The X_P is even in Φ, while Y_P is odd in Φ.

$$X_P(\Phi,\theta) = A\cos\left(\Phi\cos\left(\theta-\theta_{opt}\right)\right)+C$$

$$Y_P(\Phi,\theta) = A\sin\left(\Phi\cos\left(\theta-\theta_{opt}\right)\right)+C$$

to obtain the parameters Φ and θ_{opt}. A fits the normalized readout contrast (expected to be 1) and C fits an offset that is expected to be zero. The expected dependence of X_P and Y_P is shown in Fig. S5.

In order to determine B_{max} from the fit parameters, we use the analytical model of the exponential rise/fall shapes described in Supplementary Section 4.1, under which

$$B_{max} = \beta * \Phi/(0.5 * 8N\tau * 2\pi\gamma)$$

where β is derived from θ_{opt} (Fig. 7 main text), the factor of 0.5 is the duty cycle of photoexcitation, N is the number of XY8 block repetitions, and γ is the gyromagnetic ratio of the NV center electron spin.

4.3 Phase broadening

Since the photocurrent magnitude is dependent on the distance from the NV center location to the red excitation spot, averaging data over the ensemble of NVs in the green spot size (*FWHM* ~0.5 μm) will in general introduce a Gaussian distribution of Φ for the probed NV ensemble. Similarly, long-timescale drift, especially thermal drift due to heating from microwave pulses, could broaden the distribution of measured XY8 signal. We account for all sources of broadening in a single Gaussian average of signal width σ:

$$\overline{X}(\Phi,\theta,\sigma) = \frac{1}{\sqrt{2\pi}\sigma}\int X(\Phi,\theta)\,exp\left(-\frac{(\Phi'-\Phi)^2}{2\sigma^2}\right)d\Phi' = exp\left(-\cos\left(\theta-\theta_{opt}\right)^2\sigma^2/2\right)X(\Phi,\theta)$$

And likewise:

$$\overline{Y}(\Phi,\theta,\sigma) = exp\left(-\cos\left(\theta-\theta_{opt}\right)^2\sigma^2/2\right)\,Y(\Phi,\theta).$$

We illustrate our fits with two example data sets from the R_X linecut for B_{ext} parallel to [111] shown in Fig. 4a of the main text. All errorbars reported in our paper are 95% confidence intervals.

As is evident from Fig. S6, incorporation of a signal width σ improves the fit particularly for small values of $|R|$, when the green (probe) and red (excitation) beams overlap. This is consistent with the fact that the photocurrent distribution changes most rapidly versus distance near $R = 0$. The signal width decreases for larger values of R, and does not make an appreciable difference on the extracted value of the maximal phase Φ. For small signals, averaging over a distribution of acquired phases tends to increase the oscillation amplitude in X_P (which is insensitive to the sign of ϕ) and decrease the oscillation amplitude in Y_P (which is sensitive to the sign).

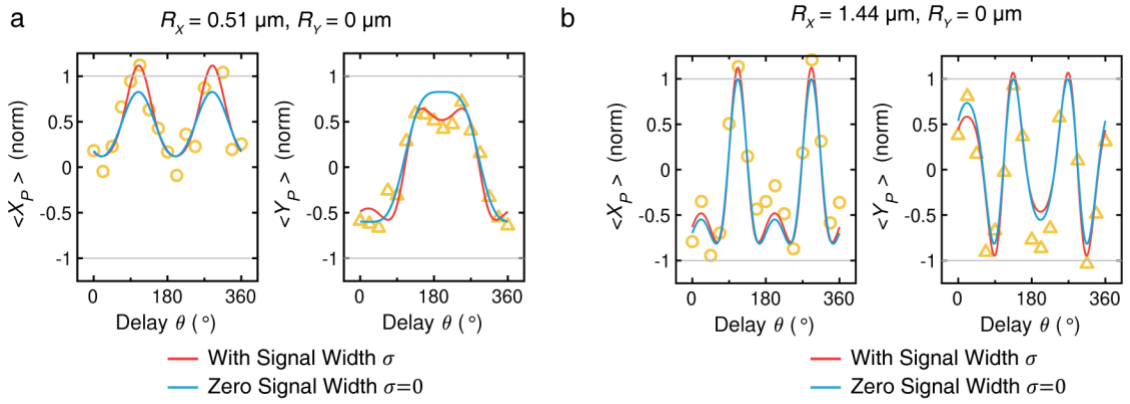

Fig. S6. Illustration of data fits. X_P and Y_P are fit to functions which either incorporate broadening due to a width σ in the acquired phase (red curves) or which have no phase broadening (blue curves). a) Data for $R_x = 0.51\,\mu m$. b) Data for $R_x = 1.44\,\mu m$. The extracted fit parameters are given below:

$R_x = 0.51$ μm, with Signal Width	$R_x = 0.51$ μm, No Signal Width	$R_x = 1.44$ μm, with Signal Width	$R_x = 1.44$ μm, No Signal Width
$A = 1.08 \pm 0.18$	$A = 0.71 \pm 0.11$	$A = 1.06 \pm 0.25$	$A = 0.91 \pm 0.14$
$C = 0.03 \pm 0.08$	$C = 0.11 \pm 0.10$	$C = 0.06 \pm 0.10$	$C = 0.09 \pm 0.10$
$\Phi = (-1.39 \pm 0.22)$	$\Phi = (-1.56 \pm 0.25)$	$\Phi = (-3.91 \pm 0.22)$	$\Phi = (-3.93 \pm 0.20)$
$\phi = (19 \pm 5)°$	$\phi = (19 \pm 8)°$	$\phi = (21 \pm 3)°$	$\phi = (22 \pm 3)°$
$\sigma = 1.25 \pm 0.28$		$\sigma = 0.83 \pm 0.50$	

4.4 Additional data analysis

In Fig. 3c of the main text, the data sets are fit to a saturation curve model:

$$\Phi(P) = \frac{\Phi_{sat} P}{P + P_{sat}}$$

Here, Φ_{sat} is the maximum achievable phase and P_{sat} is the characteristic optical power (at which half the maximum phase is reached).

We make an additional comment on Fig. 4a of the main text where the direction of the external magnetic field B_{ext} is reversed. When B_{ext} is flipped, the dispersion with field of the lower branch $m_s = |-1\rangle$ is flipped as well (equivalently, the addressed NV axis is flipped). Therefore, if the magnetic field induced by the photocurrents is also reversed, then the two negative signs will cancel and the probed NV center actually picks up the same phase. If the probed NV center picks up the opposite phase, then it would mean that the magnetic field of the photocurrents stayed the same (see Fig. S8). We measure the same acquired phase on the NV center when B_{ext} is flipped, thus indicating that the photocurrents actually reversed. In Fig. 4a, we choose to plot B_{max} relative to the fixed laboratory frame, rather than along the NV axis which also flips with field.

In Fig. 6 of the main text, the data sets are fit to a linear background with a Gaussian dip. A simple simulation averaging over random phases shows a Gaussian to be a good approximation up to moderate maximum phase.

Section 5: Control and Supplemental Data

5.1 Signal without 1-*L* MoS_2 using 677 nm excitation

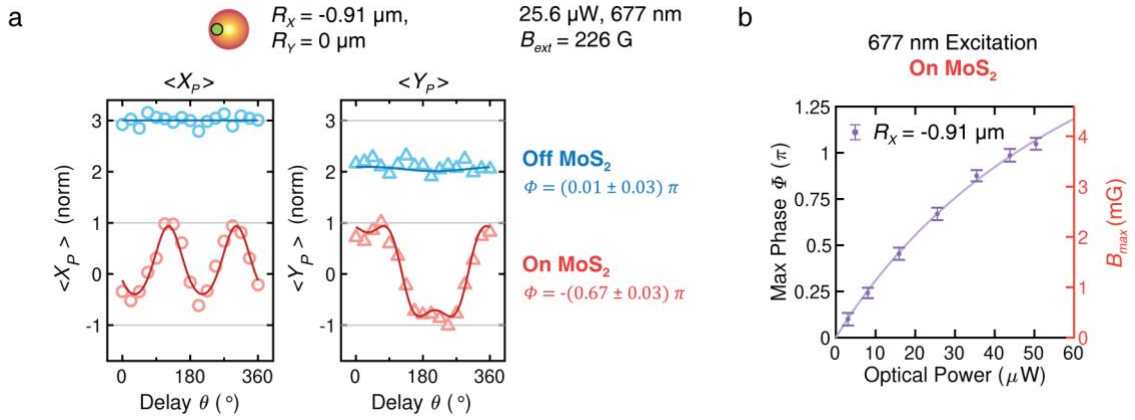

Fig. S7. Control experiment demonstrating necessity of MoS_2 for the photocurrent signal. a) Top traces (blue): X_P and Y_P for the photocurrent sensing sequence run for NV centers in an area where MoS_2 does not cover the diamond. No oscillations are measured, consistent with negligible interaction of the 677 nm excitation with diamond. The extracted phase Φ is indistinguishable from 0. Bottom traces (red): Identical photocurrent sensing sequence but run for NV centers in an area covered by MoS_2. Oscillations appear in X_P and Y_P due to the generation of an ac photocurrent. b) Dependence of the maximal acquired phase Φ on the optical power of the 677 nm excitation laser. The qualitative behavior is similar to 661 nm excitation shown in Fig. 3c of the main text. Thus, we show that photocurrent generation works for multiple excitation wavelengths. Since the photocurrent is due to the photothermoelectric effect, it only depends on the absorption of the excitation wavelength by MoS_2.

5.2 Phase acquisition using superposition of $|0\rangle$ and $|+1\rangle$ states

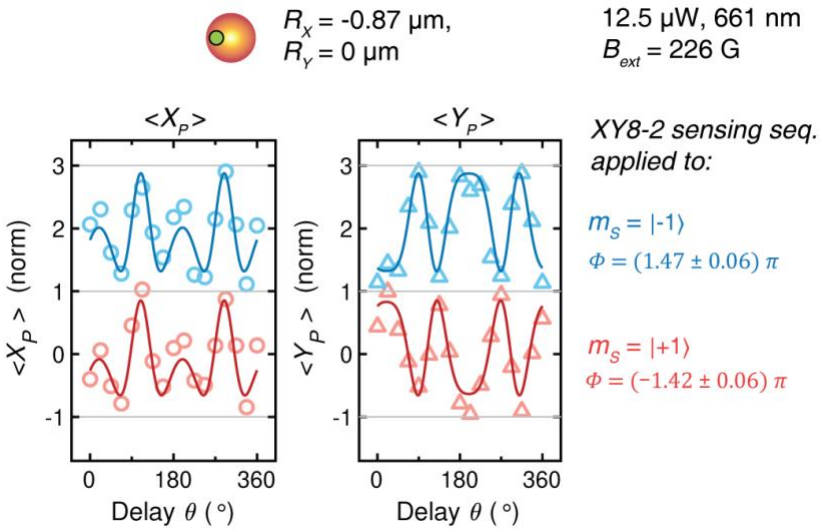

Fig. S8. Data demonstrating magnetic origin of the acquired phase by the NV center. Top traces (blue): X_P and Y_P for the photocurrent sensing sequence using an initial state $|\psi_{-1}\rangle = 1/\sqrt{2}\ (|0\rangle + |-1\rangle)$. The extracted maximal phase is $\Phi = (1.47 \pm 0.06)\,\pi$. Bottom traces: X_P and Y_P for the identical sensing sequence using $|\psi_{+1}\rangle = 1/\sqrt{2}\ (|0\rangle + |+1\rangle)$. The acquired phase Φ is the negative of the data using $|\psi_{-1}\rangle$.

In principle, MoS_2-assisted heating of the diamond substrate could induce a time-periodic change in the zero-field splitting *D* and also lead to effective precession via detuning of our microwave pulses from resonance. However, the data of Fig. S8 shows that sensed signal is magnetic in origin since $|+1\rangle$ and $|-1\rangle$ acquire opposite Zeeman shifts with magnetic field. If the signal was thermal in origin (due to ac heating of the diamond), then both the $|+1\rangle$ and $|-1\rangle$ would acquire the same sign of the phase due to common shifts in the zero-field parameter *D*.

5.3 Determining τ_{rise} from θ_{opt} versus τ

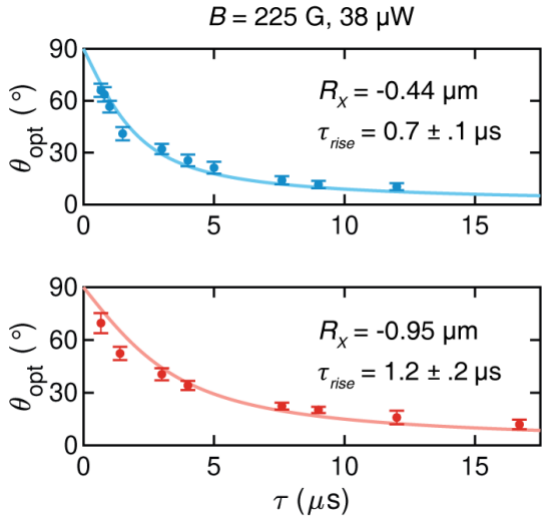

Fig. S9. Additional determination of τ_{rise} versus position by analyzing θ_{opt} from the same data sets presented in Fig. 5b of the main text. As explained in Supplementary Section 4.1, if the photocurrent rises and falls with a characteristic rise time τ_{rise}, then θ_{opt} will increase as ratio τ_{rise}/τ increases. This behavior is shown in Fig. S5b. By considering θ_{opt} rather than B_{max}, the experiment presented in Fig. 5b of the main text can also be utilized to map out the dependence shown in Fig. 7b of the main text with τ_{rise} constant and τ varying. We derive the analytical dependence for θ_{opt} assuming a pulse shape with equal rise and fall times:

$$\theta_{opt} = 180\frac{\tau_{rise}}{\tau} ln\left(\frac{2}{1+\exp\left(-\frac{\tau}{\tau_{rise}}\right)}\right)$$

We now fit θ_{opt} to the single parameter fit given above for the data sets where τ of the synchronized sensing sequence is varied. The fitted rise times τ_{rise} from θ_{opt} are consistent with the same values extracted from fitting B_{max} (Fig. 5b of main text), showing that this simple model is largely adequate. This confirms the conclusion that τ_{rise} increases for larger $|R|$. In addition, the accurate fit demonstrates that θ_{opt} can be predominantly explained by τ_{rise} of the pulse shape and does not evidence for additional delays.

5.4 Independence of τ_{rise} from the external magnetic field B_{ext}

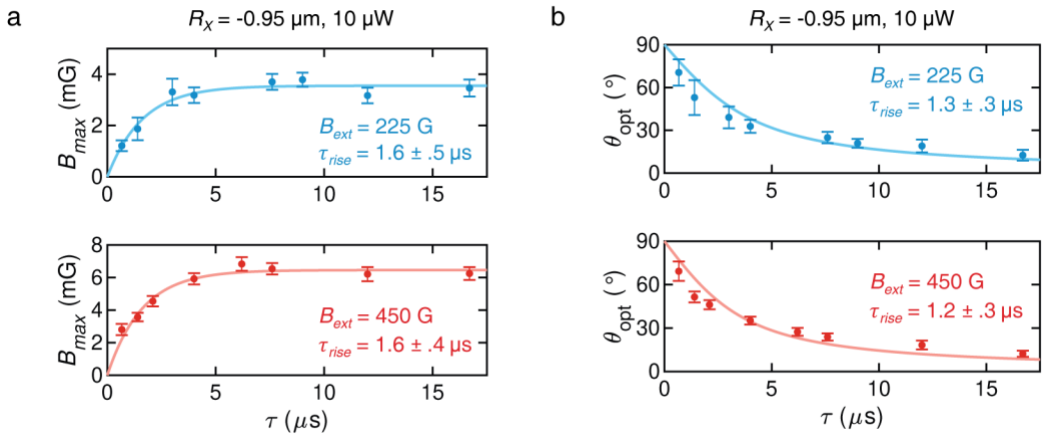

Fig. S10. Determination of τ_{rise} for two different values of the magnetic field: $B_{ext} = 225$ G (blue) and $B_{ext} = 450$ G (red). The optical power for photoexcitation of MoS_2 is 10 µW. a) Determination of τ_{rise} from B_{max} (calculated from the maximum accumulated phase Φ). b) Determination of τ_{rise} from θ_{opt}. For both methods, the fitted τ_{rise} shows no dependence on B_{ext}, which would affect carrier propagation. If the photocurrent was somehow generated non-locally (for example, at the center of the excitation beam) and propagating towards the probed spot, then τ_{rise} would be expected to depend on B_{ext}. Its independence therefore suggests that all photocurrents are generated locally by the local thermal gradient. τ_{rise} deduced from θ_{opt} tends to be slightly lower than τ_{rise} from B_{max} (although consistent within errorbar). This is likely due to the imperfection of our simple pulse shape model.

Section 6: Thermal Modeling

As explained in Appendix D of the main text, the 2D heat equation describing our system is:

$$\rho\, c_p \frac{\partial T_M(R,t)}{\partial t} - \kappa\, \frac{1}{R}\frac{d}{dR}\left[R\, \frac{dT_M(R,t)}{dR}\right] + \frac{G}{d}[T_M(R) - T_D] = f(R)$$

where $T_M(R,t)$ is the time-dependent temperature (K) of the monolayer MoS_2, R is the radial coordinate, and the rest of the parameters are given in the table below:

Density of MoS_2	$\rho = 5.06 * 10^{-15}$	$\frac{\text{kg}}{\mu\text{m}^3}$	*Ref.* [10]
Effective Specific Heat Capacity of 1L-MoS_2	$c_p(T_M) = (200 * T_M)$	$\frac{\text{J}}{\text{kg K}}$	*Match to* τ_{rise} *data*
Low Temp. Thermal Conductivity of 1L-MoS_2	$\kappa(T_M) = (0.2 * 10^{-6} * T_M)$	$\frac{\text{W}}{\mu\text{m K}}$	*Ref.* [11] *(expt)*
Thermal Interface Conductance between 1L-MoS_2 and diamond	$G = 5 * 10^{-10}$	$\frac{\text{W}}{\mu\text{m}^2\ \text{K}}$	*Ref.* [12] *(theory) for* SiO_2 *substrate*
Thickness of 1L-MoS_2	$d = 0.65 * 10^{-3}$	μm	*Ref.* [10]
Temperature of Diamond Substrate	$T_D = 6$	K	*Measured at cold-finger*
Volumetric Laser Heating Source	$f(R) = \frac{P\,\eta}{2\pi R_0^2}\frac{\alpha}{t}\exp\left(-\frac{R^2}{2\,R_0^2}\right)$	$\frac{\text{W}}{\mu\text{m}^3}$	

For the volumetric heating source, we utilize

Power measured at the back of the objective	P	W	*Measured*
Transmission Coefficient of our objective/cryostat window for 661 nm	$\eta = 0.85$		*From specs*
Absorption of 1L-MoS_2 for 661 nm excitation	$\alpha = 0.03$		*Ref.* [13,14] *(expts) for CVD* 1L-MoS_2
Gaussian Beamwidth of Excitation Beam	$R_0 = 0.45$	μm	*Measured*

We remark that due to the large number of unknown degrees for freedom and the novelty of our technique, we do not aim to extract high precision measurements of thermal constants in this current work. Our aim is to motivate our physical observations and confirm or provide order-of-magnitude estimates. Where possible, we have utilized published values. For example, the low temperature thermal conductivity of CVD-grown 1L-MoS_2 was reported in Ref. [11] for two different samples. The temperature dependence was approximately ~$T^{1.3}$ power law, reaching ~20 W/m K at 100 K, and we approximate this trend by using the linear dependence

$\kappa(T_M) = (0.2 * T_M)\ \frac{\mathrm{W}}{\mathrm{m\ K}}$. The thermal interface conductance between 1L-MoS_2 and SiO_2 was theoretically calculated in Ref. [12] to strongly decrease with temperature as $\sim T^4$. Based solely on Debye temperature mismatch, the interface conductance to diamond (which has the highest Debye temperature of all known materials) could be even lower than for SiO_2 substrates; however, exact calculations are necessary to quantify this effect. We adopt a value of $5 \cdot 10^{-4}\ \frac{\mathrm{MW}}{\mathrm{K\ m^2}}$, roughly the value for MoS_2 to SiO_2 at 10 K. To our knowledge, the low temperature heat capacity c_p for 1L-MoS_2 has not been experimentally reported in literature. Ref. [15] theoretically predicts a $\sim T^{1.1}$ phonon contribution to the heat capacity of 1L-MoS_2 below 50 K.

We estimate that $c_p(T_M) \approx (200\ \frac{\mathrm{J}}{\mathrm{kg\ K^2}} * T_M)$ is required to reproduce the microsecond-scale rise-times for the photocurrents observed in the experiment (see Appendix D). This estimate ends up significantly higher than that theoretically predicted for single crystal, single layer MoS_2 [15,16]. Excess contributions to c_p would arise from grain boundaries in our polycrystalline MOCVD sample (with grain size $\sim 3\ \mu\mathrm{m}$ contributing less than 1 grain boundary on average inside $R = 1\ \mu\mathrm{m}$), from defects due to sample storage and handling prior to placement in our cryostat (~few days), or from PMMA residue remaining from dry transfer process. Notably, a layer of cryopumped absorbates (see Fig. S3) that could well be thicker than our monolayer sample could also provide a source of heat capacity that slows down the thermal equilibration. Our experimental setup exacerbates outgassing issues, because our low-working distance objective is held at room-temperature *inside* the cryostat, without a full-coverage cold window separating it from the sample. Nevertheless, the qualitative spatial behavior seen in experiment is consistent with our thermal simulations of PTE (Fig. 9 main text). Moreover, the clear and consistent time-dependences observed for B_{max} and θ_{opt} demonstrates our technique's ability to temporally resolve photocurrent dynamics in the $\sim\mu s$ range.

Section 7: Stray Field Modeling

To model the stray field produced by the photo-Nernst vortex at the location of the probed NV centers, we integrate the field produced by current loops of continuously varying radii. Given the rotational symmetry of the experiment and the evidence pointing towards a photo-thermal mechanism, we assume the current density to be proportional to the gradient of a Gaussian temperature distribution, such that:

$$J(R) = J_0 \cdot \frac{\sqrt{e}}{\sigma_J} R \exp\left(-\frac{R^2}{2\sigma^2}\right)$$

With this parametrization, the maximum of the current density is J_0, occurring for $R = \sigma_J$. The stray field produced by this current distribution is

$$\vec{B}(\vec{x}) = \int_0^\infty \overrightarrow{\delta B}(R, \vec{x})\, dR$$

where $\overrightarrow{\delta B}(R, \vec{x})$ is the field produced at the location $\vec{x}$ by the infinitesimal current loop of amplitude $J(R)$ for radius R. The vector $\vec{x} = (R_x, R_{y,} - 40\ \mathrm{nm})$, where R_x and R_y are the coordinates of the scan and the z-component is the depth of the NV center, taken to be 40 nm based on our nitrogen implantation conditions.

We next project $\vec{B}(\vec{x})$ onto the NV axis. In order to produce better quantitative match to the experimental data, we incorporate several degrees of freedom, which do not fundamentally change the conclusions of the paper. First, to account for sample miscut or mounting inaccuracy, we assume possible misalignment between the NV axis and the *x* and *y* coordinate axes of the beam sweep ($\phi_{misalign}$). In addition, we incorporate possible misalignment (deviating from 54.7°) between the NV axis and the normal direction to the MoS_2 plane ($\theta_{misalign}$). As will be explained later, $\theta_{misalign}$ can also be interpreted as a phenomenological parameter that simulates deviations from perfect rotational symmetry of the excitation beam. This gives:

$$B_{NV}(\vec{x}) = \left(R_z\left(\phi_{misalign}\right) \cdot R_Y\left(\theta_{misalign}\right) \cdot \hat{n}_{NV}\right) \cdot \vec{B}(\vec{x}) \equiv B_{max}(\vec{x})$$

where $\hat{n}_{NV} = \left[\sqrt{2}\ 0\ 1\right]'/\sqrt{3}$. Finally, we assume an uncertainty in our positional measurements (Δ_X, Δ_Y), which would cause our R_X scan to not exactly occur for $R_Y = 0$, and vice versa.

We remark that by performing our measurements of B_{NV} over a full 2D area (rather than the orthogonal linecuts here), we would be able to utilize Biot-Savart inversion (Ref. 23-24 of the main text) to determine the two-dimensional current density $\vec{J}(\vec{r})$ uniquely, without assuming the modeled form for $J(R)$. Reducing the pixel time through photonic engineering and improved NV coherence times should allow this to be possible in future experiments.

We first compare the current density used in matching the data in Fig. 4a,b of the main text to thermal modeling of the temperature gradient summarized in Figs. 8 and 9 of the main text.

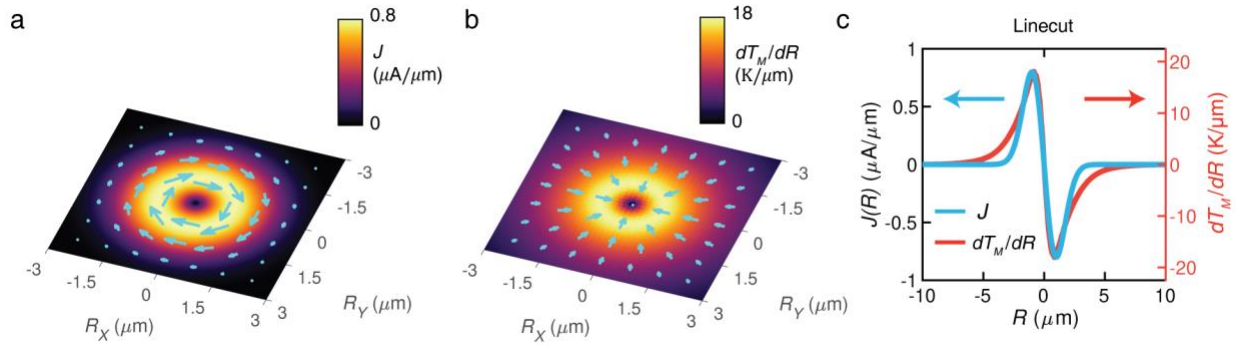

Fig. S11. Comparison of the spatial distributions of the assumed $J(R)$ and the simulated thermal gradient. a) Photocurrent distribution $J(R)$ using $J_0 = 0.8$ μA/μm and $\sigma_J = 1.0$ μm. b) Distribution of the thermal gradient $dT_M/dR\ (R)$ in the thermal model at the end of the $\tau = 7.6$ μs pulse for an optical excitation power of 25 μW (Fig. 9b). c) The radial linecuts show good correspondence between the spatial shape of the assumed $J(R)$ and simulated $dT_M/dR\ (R)$ from heat-equation modeling.

We now present the stray field projected onto the NV axis for sweeps along R_X and R_Y. Shown are both the stray field under ideal conditions (no misalignment angles or positional offsets), as well as the stray field under conditions used to approximate the data in Fig. 4a,b of the main text.

The parameters for the panels are:

a) $J_0 = 0.8$ μA/μm; $\sigma_J = 1.0$ μm; $(\phi_{misalign}, \theta_{misalign}) = (0,0)$; (Δ_X, Δ_Y) = (0,0)
b) $J_0 = 0.8$ μA/μm; $\sigma_J = 1.0$ μm; $(\phi_{misalign}, \theta_{misalign}) = (0,0)$; (Δ_X, Δ_Y) = (0,0)
c) $J_0 = 0.8$ μA/μm; $\sigma_J = 1.1$ μm; $(\phi_{misalign}, \theta_{misalign}) = (-5°, 8°)$; (Δ_X, Δ_Y) = (0.1,-0.1) μm
d) $J_0 = 0.8$ μA/μm; $\sigma_J = 0.9$ μm; $(\phi_{misalign}, \theta_{misalign}) = (-5°, 8°)$; (Δ_X, Δ_Y) = (0.25,-0.1) μm

The red solid lines in c) and d) of Fig. S12 are reproduced as the solid simulation curves in Fig. 4a,b of the main text. We emphasize that the qualitative signatures of the vortex current density are not changed at all by our assumption of experimental non-idealities. While the sample mounting or sample miscut (±3°) could account for a large portion for $\phi_{misalign}$ (misalignment between our scan axes and the in plane projection of the NV axis), $\theta_{misalign} = 8°$ (misalignment between the MoS_2 and diamond surface normal) is too large to be physically reasonable. To understand this, we consider that $\theta_{misalign}$ tilts the NV axes further oblique (away from normal) and thus enhances the asymmetry of the stray field projected onto the NV axis for positive and negative R_x. Equivalently, this effect could arise if the left and right sides of the excitation beam do not have the same intensity. Thus, $\theta_{misalign}$ serves as a proxy for the lack of perfect circular symmetry for the excitation beam intensity, which would otherwise be difficult to exactly model.

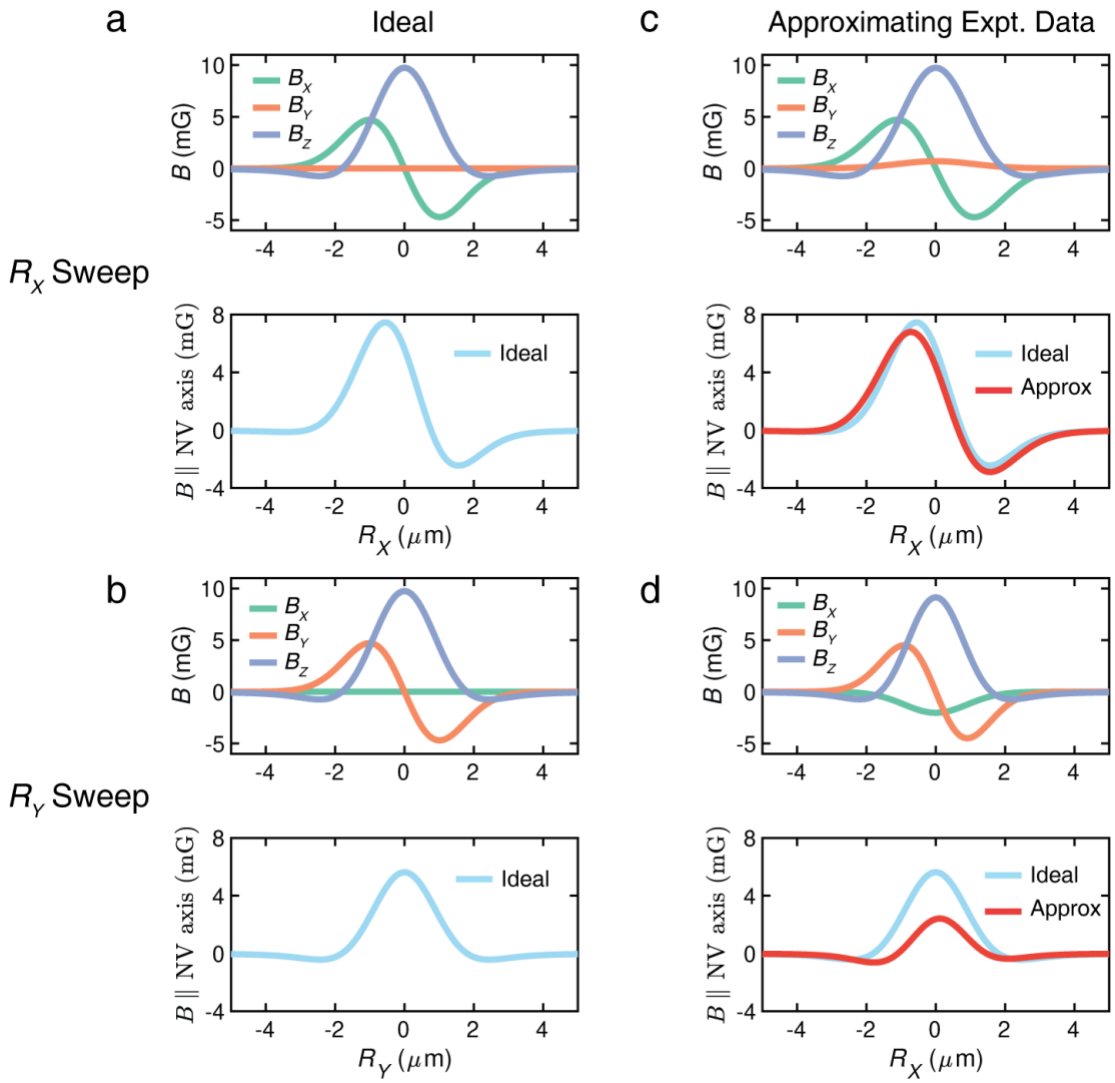

Fig. S12. The components (B_x, B_y, B_z) of the total field $\vec{B}$ and its projection B_{NV} onto the NV axis produced by the vortex current density $J(R)$ versus position. a,c) Sweep of R_X, ideal versus misaligned. b, d) Sweep of R_Y, ideal versus misaligned.

Section 8: Proposal to Extend Temporal Resolution

The maximum frequency for an ac field that can be directly measured by our NV ac magnetometry sequence is ~50 MHz, which is not sufficient to resolve relaxation transients of ultrafast photocurrents (generally in the femtosecond to picosecond range) [17–19]. Fortunately, resolving ultrafast dynamics usually does not rely on the bandwidth of the electrical or optical detector, but on controlling the delay between pump and probe excitation lasers. Our quantum lock-in technique is fully compatible with pump-probe excitation to achieve high temporal resolution. Here, we propose a straightforward modification by replacing the continuous wave excitation laser of our current work with an ultrafast pulsed laser that will enable the investigation of sub-picosecond photocurrent dynamics in materials by ac NV magnetometry.

Fig. S13a shows a typical setup [19] for measuring ultrafast photocurrent dynamics by electrical detection – a beam-splitter splits the output of a pulsed femtosecond laser, after which a delay stage controls the relative time delay Δt (to sub-picosecond resolution) between the split "pump" and "probe" beams. The actual electrical measurement is obtained via lock-in by chopping both beams at slow ~1 kHz frequencies, and plotting the lock-in signal versus the time-delay Δt of the probe pulse. In essence, the response of the sample to multiple repeated pulse pairs is integrated over much longer time scales. Ultrafast time resolution is obtained because the photoresponse of the sample to additive energy from the pulse pairs is nonlinear, saturating for close pulse spacing and recovering with the lifetime of the photoexcited carriers. This scheme is typical of virtually all measurements of ultrafast photocurrent dynamics [17–19], as there is no intrinsic detector with the gain-bandwidth performance to directly measure sub-picosecond photocurrents.

The NV "quantum" lock-in protocol is fully compatible with the above scheme as it is solely meant to replace the method of detection – from electrical to magnetic, while the time-resolution is determined by the method of excitation. As shown in Fig. S13b, to gain time resolution, we need to replace the continuous wave excitation source of this current work with an ultrafast pulsed laser and introduce a delay line as in Fig. S13a. Our electro-optic modulator will then allow us to modulate the global envelope for the pump and probe pulses ON/OFF at ~100 kHz. Meanwhile, RF π-pulses applied to the NV center synchronized with this ~100 kHz modulation envelope ($\theta_{opt} = 0$ for these fast photocurrents) will enable the precession due to multiple fast photocurrent pulses to be integrated (for varying pump-probe delays), while rejecting noise at other frequencies and extending the NV coherence time. The accumulated phase Φ due to the magnetic signal is expected to display the same auto-correlation curve in the pump-probe delay Δt as for the electrical signal, revealing the relaxation dynamics with sub-picosecond resolution (Fig. S13b). These ultrafast measurements can be made as a function of relative displacement between the probed NV center's location and the excitation spot, revealing details not possible by existing techniques.

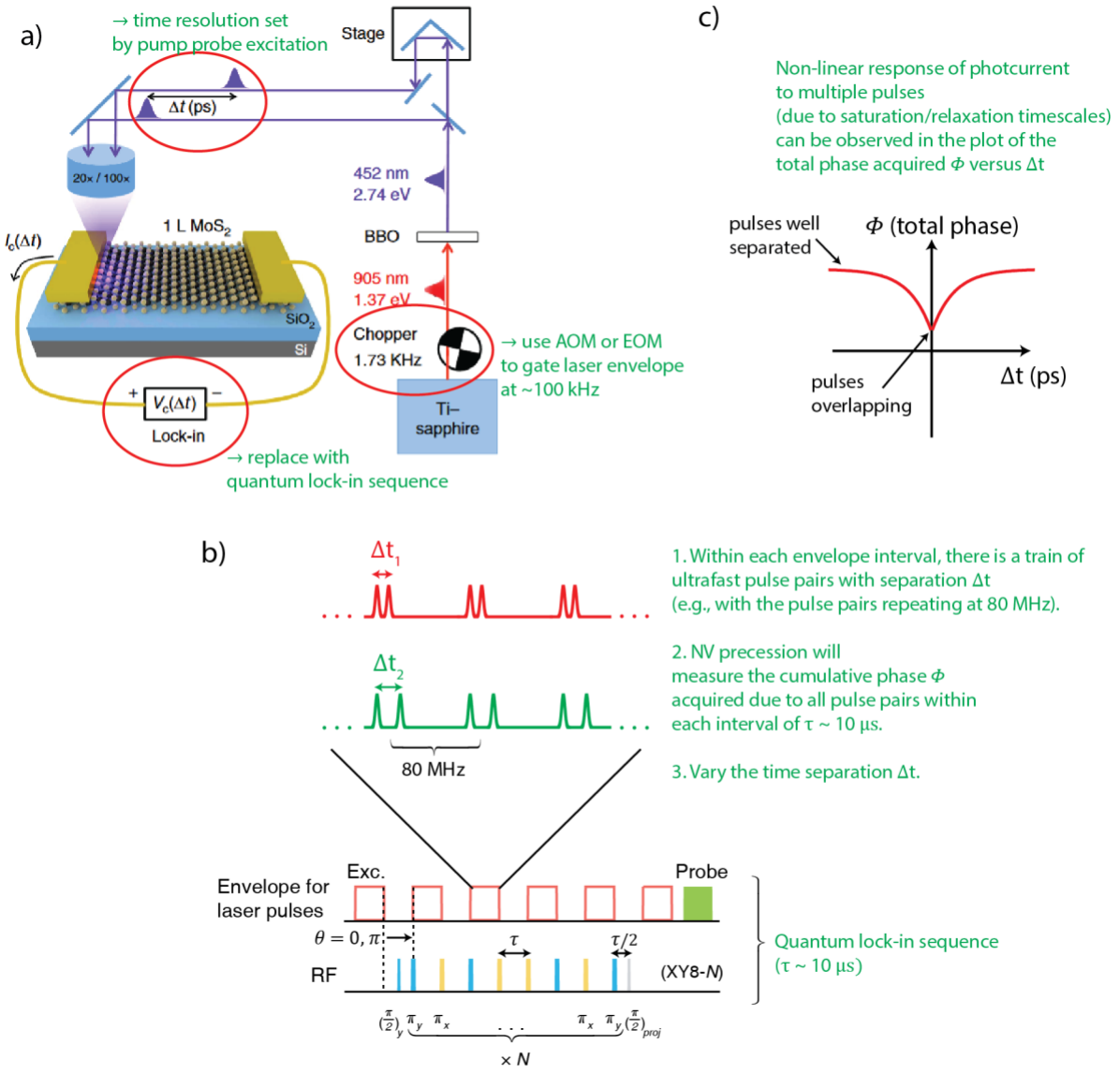

Fig. S13. a) Typical experimental schematic from Ref. [19] for the electrical detection of ultrafast photocurrent dynamics. The circled elements show that there is high time resolution (~ps) for the excitation pulses, while detection by lock-in at the chopper frequency occurs on much slower time scales (~ms). b) Utilizing pump-probe pulses with the NV ac magnetometry sequence. Since the response time and repetition rate of the photocurrent pulses are nearly instantaneous compared to the envelope frequency (~100 kHz), maximal "in-phase" response Φ will occur for a relative delay $\theta = 0°$ (or 180°). c) The phase Φ integrated over multiple pulse pairs is detected by NV magnetometry. Plotting Φ versus the pump-probe delay Δt reveals the ultrafast relaxation dynamics.

Supplementary References

[1] K. Kang, S. Xie, L. Huang, Y. Han, P. Y. Huang, K. F. Mak, C.-J. Kim, D. Muller, and J. Park, Nature **520**, 656 (2015).

[2] K. Kang, K.-H. Lee, Y. Han, H. Gao, S. Xie, D. A. Muller, and J. Park, Nature **550**, 229 (2017).

[3] H. Hattab, A. T. N'Diaye, D. Wall, C. Klein, G. Jnawali, J. Coraux, C. Busse, R. van Gastel, B. Poelsema, T. Michely, F.-J. Meyer zu Heringdorf, and M. Horn-von Hoegen, Nano Lett. **12**, 678 (2012).

[4] P. Jacobson and S. Stoupin, Diam. Relat. Mater. **97**, 107469 (2019).

[5] L. Zhang, Z. Lu, Y. Song, L. Zhao, B. Bhatia, K. R. Bagnall, and E. N. Wang, Nano Lett. **19**, 4745 (2019).

[6] J.-P. Tetienne, R. W. de Gille, D. A. Broadway, T. Teraji, S. E. Lillie, J. M. McCoey, N. Dontschuk, L. T. Hall, A. Stacey, D. A. Simpson, and L. C. L. Hollenberg, Phys. Rev. B **97**, 085402 (2018).

[7] T. Wolf, P. Neumann, K. Nakamura, H. Sumiya, T. Ohshima, J. Isoya, and J. Wrachtrup, Phys. Rev. X **5**, 041001 (2015).

[8] S. Wu, L. Wang, Y. Lai, W. Shan, G. Aivazian, X. Zhang, T. Taniguchi, K. Watanabe, D. Xiao, C. Dean, J. Hone, Z. Li, and X. Xu, Sci. Adv. **2**, e1600002 (2016).

[9] R. Yan, J. R. Simpson, S. Bertolazzi, J. Brivio, M. Watson, X. Wu, A. Kis, T. Luo, A. R. Hight Walker, and H. G. Xing, ACS Nano **8**, 986 (2014).

[10] M. Buscema, M. Barkelid, V. Zwiller, H. S. J. van der Zant, G. A. Steele, and A. Castellanos-Gomez, Nano Lett. **13**, 358 (2013).

[11] M. Yarali, X. Wu, T. Gupta, D. Ghoshal, L. Xie, Z. Zhu, H. Brahmi, J. Bao, S. Chen, T. Luo, N. Koratkar, and A. Mavrokefalos, Adv. Funct. Mater. **27**, 1704357 (2017).

[12] Z.-Y. Ong, Y. Cai, and G. Zhang, Phys. Rev. B **94**, 165427 (2016).

[13] D. Dumcenco, D. Ovchinnikov, K. Marinov, P. Lazić, M. Gibertini, N. Marzari, O. L. Sanchez, Y. Kung, D. Krasnozhon, M. Chen, S. Bertolazzi, P. Gillet, A. Fontcuberta i Morral, A. Radenovic, and A. Kis, ACS Nano **9**, 4611 (2015).

[14] J. J. Bae, H. Y. Jeong, G. H. Han, J. Kim, H. Kim, M. S. Kim, B. H. Moon, S. C. Lim, and Y. H. Lee, Nanoscale **9**, 2541 (2017).

[15] D. Saha and S. Mahapatra, Physica E **83**, 455 (2016).

[16] J. Su, Z. Liu, L. Feng, and N. Li, J. Alloys Compd. **622**, 777 (2015).

[17] A. Urich, K. Unterrainer, and T. Mueller, Nano Lett. **11**, 2804 (2011).

[18] N. M. Gabor, Z. Zhong, K. Bosnick, and P. L. McEuen, Phys. Rev. Lett. **108**, 087404 (2012).

[19] H. Wang, C. Zhang, W. Chan, S. Tiwari, and F. Rana, Nat. Commun. **6**, 8831 (2015).